

Refactoring the MPS/University of Chicago Radiative MHD (MURaM) Model for GPU/CPU Performance Portability Using OpenACC Directives

Eric Wright
University of Delaware
Newark, Delaware
efwright@udel.edu

Damien Przybylski
Max Planck Institute for
Solar System Research
Gottingen, Germany
przybylski@mps.mpg.de

Matthias Rempel
National Center of
Atmospheric Research
Boulder, Colorado
rempel@ucar.edu

Cena Miller
National Center of
Atmospheric Research
Boulder, Colorado
cmille73@ucar.edu

Supreeth Suresh
National Center of
Atmospheric Research
Boulder, Colorado
ssuresh@ucar.edu

Shiquan Su
National Center of
Atmospheric Research
Boulder, Colorado
shiquan@ucar.edu

Richard Loft
National Center of
Atmospheric Research
Boulder, Colorado
loft@ucar.edu

Sunita
Chandrasekaran
University of Delaware
Newark, Delaware
schandra@udel.edu

ABSTRACT

The MURaM (Max Planck University of Chicago Radiative MHD) code is a solar atmosphere radiative MHD model that has been broadly applied to solar phenomena ranging from quiet to active sun, including eruptive events such as flares and coronal mass ejections. The treatment of physics is sufficiently realistic to allow for the synthesis of emission from visible light to extreme UV and X-rays, which is critical for a detailed comparison with available and future multi-wavelength observations. This component relies critically on the radiation transport solver (RTS) of MURaM; the most computationally intensive component of the code. The benefits of accelerating RTS are multiple fold: A faster RTS allows for the regular use of the more expensive multi-band radiation transport needed for comparison with observations, and this will pave the way for the acceleration of ongoing improvements in RTS that are critical for simulations of the solar chromosphere. We present challenges and strategies to accelerate a multi-physics, multi-band MURaM using a directive-based programming model, OpenACC in order to maintain a single source code across CPUs and GPUs. Results for a 288³ test problem show that MURaM with the optimized RTS routine achieves 1.73x speedup using a single NVIDIA V100 GPU over a fully subscribed 40-core Intel Skylake CPU node and with respect to the number of simulation points (in millions) per second, a single NVIDIA V100 GPU is equivalent to 69 Skylake cores. We also measure parallel performance on up to 96 GPUs and present weak and strong scaling results.

ACM Reference Format:

Eric Wright, Damien Przybylski, Matthias Rempel, Cena Miller, Supreeth Suresh, Shiquan Su, Richard Loft, and Sunita Chandrasekaran. . Refactoring the MPS/University of Chicago Radiative MHD (MURaM) Model for

GPU/CPU Performance Portability Using OpenACC Directives. In *Proceedings of . ACM*, New York, NY, USA, 12 pages.

1 OVERVIEW

The MURaM (Max Planck University of Chicago Radiative MHD) code [37, 38, 48] is one of the primary solar models used for simulations of the upper convection zone, photosphere (visible surface of the sun) and corona. MURaM simulations have contributed substantially to our understanding of solar phenomena ranging from the origins of quiet sun magnetism, the structure and evolution of sunspots and active regions, to solar flares and the initiation of coronal mass ejections. MURaM also plays a key role in interpreting high resolution solar observations. With the construction of the Daniel K. Inouye Solar Telescope (DKIST), an NSF investment [33] exceeding \$300 million, resolution of ground based observational solar physics is poised to take an order of magnitude leap forward.

Radiation transport is a key component in realistic models of the solar atmosphere. In order to capture the frequency dependence of opacity in a cost effective way, spectral lines are combined in bands according to their strength Nordlund [32] (and sometimes also frequency) and average opacities are computed for each band (typically 4-12). The radiation transport is then performed for each band instead of hundred thousands of individual frequency points. But even with this substantial simplification, radiation transport in multiple bands can consume more than 90% of the computing time for photospheric simulations. As a consequence many simulations have been performed with a single "gray" band, which limits direct comparability with observations. A speedup of radiation transport will make multi-band radiation transport possible as the routine option. However, radiation transport becomes even more challenging when applied in the chromosphere.

The solar chromosphere, lying between the photosphere and the transition to the corona, is one of the least understood parts of the Sun. It is difficult to observe; as it is only visible in the cores of strong lines where the signal to noise ratio is low and the magnetic field diagnostics available are relatively poor. High resolution observations with DKIST will soon allow us to observe the chromosphere in greater detail than ever before. The theoretical

Permission to make digital or hard copies of part or all of this work for personal or classroom use is granted without fee provided that copies are not made or distributed for profit or commercial advantage and that copies bear this notice and the full citation on the first page. Copyrights for third-party components of this work must be honored. For all other uses, contact the owner/author(s).

© Copyright held by the owner/author(s).

treatment of the chromosphere is equally challenging, as none of the usual assumptions can be used. Neither radiation, nor the ionisation state of atoms can be treated in local thermodynamic equilibrium (LTE), in which the source function is simply given by the temperature dependent Planck function and population levels can be calculated with the Saha-Boltzman equation [4].

The primary requirement to correctly model the structure and dynamics of the chromosphere is the inclusion of non-equilibrium atomic populations, primarily hydrogen. Because the timescales of hydrogen ionisation and recombination in the chromosphere are of the same order as the dynamical timescales, it is a non-equilibrium problem. This requires evolving the ionisation state of the atoms as they are advected by bulk plasma motions, and then calculation of the excitation and de-excitation by collisional and radiative processes. A module to track the non-equilibrium evolution of hydrogen, using a simplified 1D radiation field, is now available for the MURaM code and increases the computational cost by about a factor of 5. Extending the module to perform realistic simulations of the chromosphere will require a thorough treatment of the radiation field, including multiple wavelengths covering all the important atomic transitions.

The problem under study, MURaM is capable of simulating the coupled solar atmosphere from the upper convection zone into the lower solar corona, covering a density stratification of more than 25 scale heights. This makes MURaM a crucial tool for studying how magnetic field emerging from the solar interior is energizing the solar atmosphere and is leading to rapid release of energy in form of flares and coronal mass ejections. Figure 1 shows an example of such a simulation from Cheung et al. [13]. Currently these simulations are "stand-alone" setups that are inspired by solar events, but do not aim at modeling observed solar events in detail. Using these simulations in the future as a utility to study the solar drivers of space weather events will require data ingestion through boundary driving or full data assimilation and the ability to run such simulations in real-time.

In summary, future science applications of the MURaM code will focus on detailed studies of the coupled solar atmosphere as well as data-driven simulations of solar events. This requires the combination of (1) higher resolution, (2) more sophisticated physics in terms of radiation transport and (3) ensemble simulations. The resulting increased demand in computing speed cannot be achieved with traditional CPU based systems.

1.1 Motivation

The above scientific advancements can be achieved by a combination of two classes of simulations: (1) High resolution simulations in smaller domains with more detailed physics that allow for the direct comparison with observations that will be available from DKIST. Here it is specifically critical to **speed up radiation transport** such that multi-band simulations become the norm and more detailed physics can be added in the near future. (2) Low resolution simulations in large domains with the standard physics of MURaM in order to simulate (and predict) observed solar space weather events. For these simulations it is critical to **reach the real-time threshold** in order to allow for data-assimilative simulations in the future. Starting from the current CPU baseline of the code, an

increase of computational capabilities by 1-2 orders of magnitude is needed.

To achieve these ambitious science goals, migration from petascale to exascale computing is clearly required. In the context of the US Department of Energy (DoE)-led exascale program [19], this means focusing on Graphics Processing Units (GPUs). There are several possible language/compiler pathways to exascale computing with GPUs: vendor-specific languages like CUDA [34], directive-based standards such as OpenMP offloading model above [44] and OpenACC [24]; and domain-specific languages (DSL) such as Stella and its successor GridTools [22].

The project to refactor MURaM for GPUs had multiple goals. First and foremost, we sought to improve the throughput of the model, as measured by site updates per second, or simulated seconds per wall clock second to the maximum extent possible. The project's target throughput speedup was parity between one NVIDIA V100 GPU and 100 Intel Xeon v4 processor cores [42]. Experience refactoring similar models suggested that this speed-up was achievable for well-implemented code with sufficient data parallelism to saturate the GPUs. Our secondary goal was maintainability, by preserving portability of the model between CPUs and GPUs to the maximum extent possible. Finally, we sought, as a tertiary goal, performance-portability: namely, finding a maintainable implementation that did not compromise (significantly) model performance on CPUs or GPUs. At the time this project began in early 2018, the directive-based parallelization approach appeared to offer the best prospect of meeting the first two goals, while performance portability was an open question. Of the directive-based systems, OpenACC [24] was deemed to be the most production ready in 2018.

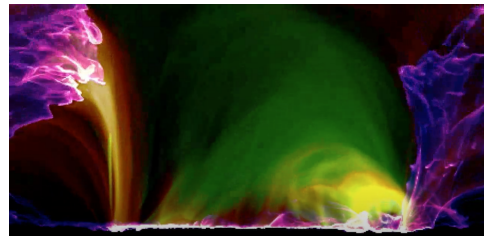


Figure 1: Data inspired simulation of a solar eruption. Presented is a still image from this outreach movie [2] that is based on Cheung et al. [13].

The directive-based programming model, OpenACC has been widely used in the past several years to migrate large scale applications demonstrating maturity and stability with the compiler implementations of the high level features. Some of the large (including production) applications that uses OpenACC include MPAS [49], ANSYS [40], Icosahedral non-hydrostatic (ICON) [41], LQCD Monte Carlo [7], and VASP [30].

OpenMP [12] also a directive-based programming model was predominantly targeting shared memory architectures since its inception in 1999. Since 2013, OpenMP has been supporting accelerators. While some applications such as GenASiS [8], Pseudo-Spectral Direct Numerical Simulation-Combined Compact Difference (PSDNS-CCD3D) [14] QMCPack [26], GAMESS [29], and other mini-application such as minisweep [47], SU3 [16] have been ported to the OpenMP offloading model, we observed that the compiler

implementations of the offloading features [18] are not yet fully mature and stable enough to tackle MURaM especially when we started the code development of MURaM in early 2018. To that end, MURaM uses OpenACC [11].

1.2 Contributions

- Specific GPU algorithmic enhancements, namely: asynchronous programming, loop fusion, and array replication, to the method of discrete ordinates used in MURaM’s radiation transport model. Radiation transport is the single most expensive part of most astrophysical codes, so these optimizations are broadly applicable across astrophysics.
- Acceleration of the radiation transport in MURaM will in turn make routine use of multi-band radiation transport possible in solar physics models.
- Multi-band radiation transport will advance understanding of the solar chromosphere when combined with non-equilibrium treatment of atomic populations.
- Demonstration of the efficacy of the use of OpenACC directive-based approach to achieve performance-portability across CPUs and GPUs in a solar physics model.

2 MURAM ROUTINES

The primary focus of the MURaM code, a solar physics code developed over the past 2 decades, are the detailed studies of the solar atmosphere with sufficient realism to allow for forward modeling of synthetic observables from visible to EUV and X-ray emission for direct comparison with a wide range of solar observations. To this end the MURaM code is typically applied to small Cartesian local regions on the Sun with lateral and vertical simulation domains ranging from a few 1000 km to more than 100,000 km, with typical numerical grid spacings in a range of 2 – 200 km (for comparison, the solar radius is about 700,000 km). The code combines a fourth order conservative MHD scheme with short characteristics radiation transport as described in [?]. The MURaM MHD scheme uses a cell centered finite difference approach, the $\nabla \cdot \vec{B} = 0$ constraint is enforced through hyperbolic divergence cleaning [17]. The radiation transport resolves the angular dependence of the radiation field by computing rays in (typically) 24 directions based on a Carlson quadrature [10]. Radiation transport is an intrinsically non-local problem, which poses implementation challenges on distributed memory architectures. The short characteristics solver of MURaM treats radiation transport locally, by using intensities from a previous time step (or iteration) as the starting point for the ray integration on each shared memory block. Achieving global convergence requires typically 3 to 4 iterations in the radiation transport solve. The above formulation has been extensively used to study magneto-convection in the solar photosphere and upper convection zone. The code has been expanded to also include the overlying solar corona [39]. These implementations lead to a fully explicit code that can be parallelized for shared memory systems through domain decomposition and MPI communication. The major computational routines of the MURaM code, their algorithms and purpose, are summarised below:

- **MHDRES** - Calculate the right hand side of the MHD equations in conservative form. Calculate the derivatives of the fluxes using a fourth order central difference scheme.
- **TVDDIFF** - Numerical diffusion required to stabilise the solution. Calculated using a slope limited diffusion scheme.
- **EOS** - Using the density and energy from the MHD solution calculate the equation of state variables; temperature, pressure, electron number, entropy.
- **RTS** - Calculate the radiation field using the thermodynamic variables of the current MHD snapshot. A short-characteristics algorithm is used. Consists of 4 main functions:
 - Interpolate - Perform trilinear interpolation of the MHD variables from the MHD grid to the staggered RTS grid. Calculate the radiation source function and opacities to be used in the integration routines.
 - Integrate - Integrate along each ray of the quadrature.
 - Exchange - Communicate intensity information to downstream processors in the ray direction.
 - Flux - From the specific intensity calculate the average intensity and radiative fluxes.
- **DIVBCLEAN** - Diffuse and disperse numerical $\vec{\nabla} \cdot \vec{B}$ errors through a hyperbolic $\vec{\nabla} \cdot \vec{B}$ cleaning approach.
- **INTEGRATE** - Calculate the updated variables for the next stage of the Runge Kutta algorithm using the divergence of fluxes from **MHDRES** and additional source terms such as gravity radiative heating/cooling.
- **DST** - Exchange subdomain ghost cells with neighbours.
- **SYNC** - Determine the maximum time-step and synchronise the timestep between subdomains.
- **VLIM** - Dynamically adjust the velocity, energy and Alfvén velocity limits to prevent extreme cells causing overly restrictive timestep constraints.
- **BOUNDARY** - Implement the vertical boundary conditions; A stratified open boundary at the bottom with passive field advection. Upper boundary is open to outflows, the magnetic field is matched to a potential magnetic field. The latter requires fast Fourier transforms.

3 PROFILING

Code profiling reveals several metrics that show in-depth information about code performance and behaviors. There are various profiling applications that serve a variety of purposes. We have used GNU gprof, ARM MAP and NVIDIA nvprof tools during the entirety of this development process. Since the beginning of this project nvprof has been deprecated by NVIDIA and replaced with NVIDIA NSight Compute, which offers many of the same functionalities. For this paper version since many of our experiments were conducted before NSight Compute’s release, we discuss our results with nvprof.

3.1 CPU Profiling

To effectively port and optimize the performance of a code it is important to gain a high-level view of the code’s performance as is to identify areas that are most computationally intensive and consume the greatest percentage of the total runtime. Additionally,

observing the scalability of the CPU code will give insight into any overheads caused by MPI communication.

Two key metrics observed during CPU profiling would be the percentage of time spent in each routine considering a single MPI rank on a single CPU core and the MPI communication of using many CPU cores as well as multiple compute nodes. Using ARM MAP for the single core profile enabled the creation of a graphical function call graph that showed the flow of code execution as well as the percentage of runtime taken by each step. Nvprof also allows for some CPU profiling, however was primarily used to observe CPU performance side-by-side with GPU performance. ARM MAP is also used to capture the MPI communication when using multiple MPI ranks across several CPUs.

The single core profiling results are shown in Figure 2. From these results, there are three portions of the code that account for 71% of the total runtime: *MHDRES*, *TVDDIFF* and *RTS*. These profiling results are for single-band radiation transport. In multi-band applications *RTS* could be up to 12 times more expensive. The importance and functionality of these routines are described in Section 2. Since this is only showing performance of a single CPU core it gives insight as to what routines are computationally intensive without concerns of any MPI overhead. With these results we have a clear starting point of what routines should be immediately targeted for parallelization.

RTS is significantly more complicated than *MHDRES* and *TVDDIFF* as the radiation portion of the code contains many smaller sub-routines. The general techniques used to parallelize *MHDRES* and *TVDDIFF*, as well as the majority of the rest of the code, is described in detail in Section 4. The parallelization of *RTS* presented many interesting challenges and was handled very differently than the rest of the code. The parallelization of *RTS* is described in Section 5.

The MPI profiling using ARM MAP results are shown in Figure 3. In contrast to the single core profiling, additional routines like *FFTW* and *DST* affects the total runtime, with *FFTW* being the MPI version of the *FFTW* 3.8 library and *DST* communicating ghost cells through MPI. *RTS* also includes a significant amount of MPI communication. Figure 3 shows that the MPI communication within *RTS* alone accounts for 6.2% of the total runtime. Optimizing the MPI communication is an important task for the performance of both and CPU and GPU code. The inclusion of GPU-aware MPI for device-to-device direct MPI data transfers is discussed in Section 4.3 and some MPI optimizations specific to *RTS* are discussed in Section 5.3.

3.2 GPU Occupancy

GPU profiling tools can reveal important information about the achievable performance of a code. One performance metric that significantly guided our development process was the achieved and theoretical GPU occupancy. GPU occupancy for NVIDIA GPUs refers to the percentage of warps active at a given time. Theoretical GPU occupancy can be determined by examining the GPU register and shared memory usage when a kernel is compiled. Low theoretical GPU occupancy is generally caused by a kernel needing to use too many registers or too much shared memory, which results in the GPU not having enough resources to support using every warp simultaneously.

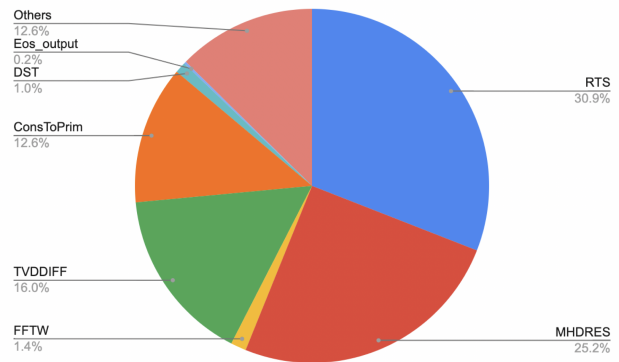


Figure 2: Single core profiling.

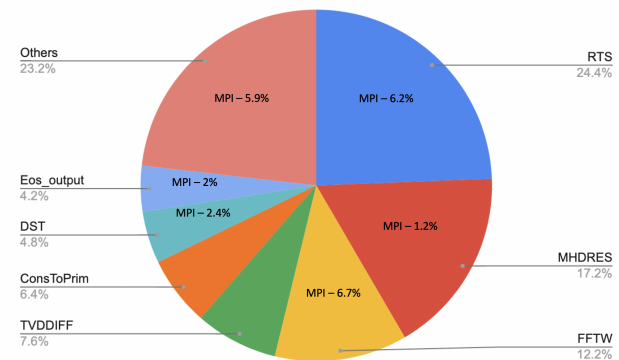


Figure 3: Multi core profiling.

Achieved GPU occupancy is simply the GPU occupancy that is observed during kernel execution. It is ideal to have theoretical GPU occupancy as close to 100% as possible and to have achieved GPU occupancy as close to the theoretical GPU occupancy as possible. There are many possible reasons for achieved occupancy to be lower than theoretical occupancy, some of which was observed in our work with MURaM. The GPU occupancy of several important kernels is shown in Figure 4 and using this metric we can identify two key performance issues within MURaM.

Firstly, many of the kernels are reaching very low theoretical occupancy, with *MHDRES* and *TVDDIFF* reaching 25% and 33% respectively. For these two kernels, the low theoretical occupancy is due to an over-allocation of GPU registers per thread. Figure 5 shows the potential theoretical occupancy of the *MHDRES* kernel when the registers per thread changes. If any more than 32 registers are allocated per thread the theoretical occupancy will go below 100%, and since *MHDRES* is compiled to use 122 registers per thread, it can only reach 25% theoretical occupancy.

This is an interesting problem in directive-based programming models, such as OpenACC, because the programmer relies on the compiler to assign GPU registers when generating the GPU code. When using a device-specific language, such as CUDA, the programmer can fine-tune this register allocation to a higher degree. In the case of *MHDRES* the PGI compiler has determined that 122 registers is the optimal number to achieve the most performance, and

incorporating a hard register limit of 32 registers sees a significant performance decrease.

Secondly, *RTS::integrate* shows a different problem where the theoretical occupancy is very high while the achieved occupancy is very low. This means that when *RTS::integrate* is compiled the number of registers and the amount of shared memory assigned is such that the GPU could potentially support every warp running simultaneously. However, in practice only 10% of those warps are used when executing the kernel. This is due to a lack of parallelism being exposed in a way that we are only able to parallelize across two dimensions of our three dimensional domain. Typically, modern GPUs are expected to perform SIMT parallelism on several millions of data points, but in this kernel we are only hitting a few ten thousands, resulting in the 10% GPU occupancy. The reasoning for this will be thoroughly elaborated on in Section 5.

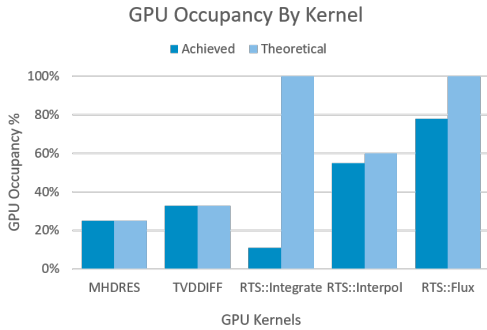


Figure 4: Theoretical and achieved GPU occupancy of various GPU kernels within MURaM.

4 DEVELOPING MURAM USING OPENACC

In this section we provide an overview of our development process with OpenACC.

4.1 Refactoring the MURaM Code

Maintaining correctness during the migration of MURaM’s large and complex code-base to support GPUs presented a challenge. To address this key issue, we chose an incremental, test-driven development approach throughout. This involved three steps: 1) identifying suitable baseline test cases; 2) creating a correctness validation build-test system; and 3) incremental migration to GPUs by applying OpenACC directives and validation of the results. It is worth noting that steps 1 and 2 required close collaboration with the solar physicists on our team.

We chose a test case with a grid size of 192x64x64 for our validation suite because it’s small enough to run on a single CPU core while still capturing the solar atmosphere from the upper convection zone into the lower solar corona and therefore testing all implemented physics in the code. We used this setup to generate the CPU reference data required to validate the GPU implementation against. During the porting and development process, its small size allowed us to quickly and repeatedly run the model for the 50 time-steps required by the validation suite without exhausting our limited cluster resources. It’s also large enough to decompose and test in different x, y, and z core layouts.

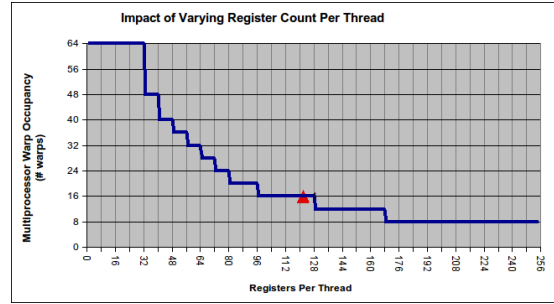


Figure 5: Effect of GPU register usage on GPU occupancy in the MHDRES and TVDDIFF kernels.

To validate correctness, we developed a validation suite which builds and runs the ported code using different combinations of processor layouts. At specific timesteps, diagnostic variable data is output into files. The test diagnostics can be compared to reference diagnostics generated by the CPU master code using a matching data set and processor layout. We defined an acceptance tolerance as the variance observed between MPI CPU runs with varying decompositions and core layouts, which is a maximum relative error margin of 1e-05. However, bit errors on the order of 1e-7 can cause large relative errors at points where the reference data is close to zero. To handle this issue, an absolute error between the diagnostic and reference data is also calculated and accepted when less than 1e-7. Figures 6 and 7 show some of the graphs generated by our validation suite. These figures are often very helpful in debugging problems that occur at predictable areas of the domain, such as at processor boundaries.

For additional correctness checking we utilized a new feature in the PGI compiler called PGI Compiler Assisted Software Testing (PCAST) [3]. This allows direct comparison of data from a reference run of the code to be compared to a current run. PCAST can be used in two modes: automatically running the CPU and GPU version of a kernel then comparing their outputs directly immediately after, or comparing the output to a previously generated PCAST output file. PCAST also has the option to generate all of these comparisons automatically with a compiler flag, however given MURaM’s code complexities, it was not straightforward to use PCAST. Regardless of the issues, we were still able to manually apply PCAST throughout the code.

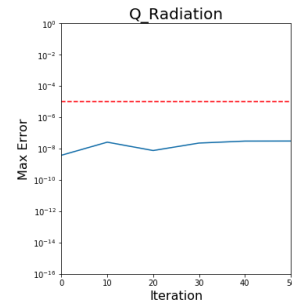


Figure 6: Maximum Relative Error in GPU calculated Q_Radiation over 50 iterations.

To implement PCAST to the code we created a wrapper macro that could be ignored based on a toggle in the code compilation, or if using a non-PGI compiler. This macro was placed before each kernel and captured the data of all of the significant input variables, as well as after each kernel and captured all significant output variables. Then the code was compiled for CPU and ran for only two timesteps to avoid creating too large of a reference file. Any future GPU runs could then be build with PCAST and compared to the CPU reference pointing out any minor discrepancy between the reference run. Additionally, PCAST includes a feature called patching that will replace any incorrect values with their reference, allowing us to see isolated errors and avoid error propagation to later tests.

In the incremental refactoring process, we initially target a single loop nest and apply OpenACC directives to have that loop run on the GPU, without focusing on any sort of optimization. Data management is also handled as locally as possible with all input variables copied to the GPU immediately before the loop and all output variables copied to the host immediately after the loop. This allows for a single isolated portion of the code to be parallelized without having any cascading effects on the rest of the code. The key benefit to this strategy is that we can ensure code correctness first and foremost before moving on to any optimizations, which can introduce new problems into the code. Once that portion of the code has been parallelized, we checked for two things. 1) ensure that the code still produces correct results, 2) verify with a profiler that the portion of code is running on the GPU and is behaving as expected.

Frequent code profiling during development gives a very important sanity check at every step of the process. It ensures that the most recent code changes are running properly on the GPU and contain any expected data movement associated with them. Some problems that this profiling can identify are kernels running significantly slower than expected, extra or unexpected data movement and low kernel performance from metrics such as occupancy or bandwidth-bound kernels. Many of these details become very important once we move past the initial parallelization and move on to optimizing the GPU code.

4.2 Optimizing Host-Device Data Movement

After every important loop was running on the GPU we began the process of eliminating redundant data movement between the host (CPU) and device (GPU). These copies are expensive, but an artifact of the careful, incremental nature of our porting strategy. As with any optimization, removing redundant data copies between neighboring kernels required re-verifying code correctness with our validation suite.

We used a GPU profiler, nvprof, to identify the data transfers occurring between kernels. Even after we had removed all the unnecessary data transfers from the code we were still observing many small data transfers happening before kernel launches. With the help of the profiler we discovered that device memory allocated with an OpenACC API function works differently than device memory allocated with an OpenACC directive, and causes there to be a small amount of data transfer before kernels where this memory is used. We are not sure exactly what within the PGI compiler causes

this, but we now solely use OpenACC directives to eliminate these small data transfers.

Every core MURaM routine is ported to the GPU with optimized data movement. Additionally, many computational kernels have been further optimized for GPU performance, and finishing optimizations on the remainder of the code is a clear future direction of the MURaM project.

4.3 Optimizing GPU-aware MPI

For the multi-GPU runs in this project we are using OpenMPI 3.1.4 that provides support for GPU-to-GPU MPI data transfers when installed on a machine with compatible hardware. To use this feature a valid GPU address pointer is passed into the MPI function call. In a language such as CUDA this is very straightforward, as the programmer explicitly manages GPU memory allocations. In OpenACC however the GPU memory allocation is hidden from the programmer by the OpenACC runtime. To expose the GPU address pointer OpenACC provides the `host_data` directive and `use_device` clause that allows interoperability with GPU-based libraries. While using GPU-aware MPI with OpenACC is very simple, verifying that device-to-device data transfers are working as expected is a challenge. The only way that we currently know to verify this functionality is by profiling the MPI GPU application using nvprof and checking explicitly that device-to-device (or DtoD) data transfers are occurring. Within our development system there was a significant amount of trouble getting OpenMPI installed with proper GPU-aware support, and several iterations of testing were required to reach the expected hardware performance level.

5 OPTIMIZING RADIATION TRANSPORT

It is well known that computing 3D radiation transport (3D-RT) is extraordinarily expensive, depending on two angular dimensions (i.e. the zenith and azimuthal angles) and three spatial dimensions. RT solvers are typically iterative, further adding to the cost. However 3D-RT is absolutely essential in many MHD and astrophysical situations, including solar physics.

In the case of MURaM's 288^3 reference test case with one band, the radiation transport solver (RTS) is the most expensive part of the calculation, accounting for nearly half the time on a single, dual-socket CPU node. More realistic, multi-node 3D radiation transport, in which the RTS must be called once per frequency band, will drive the proportion of time spent in RTS even higher.

For this reason RTS has received the most optimization effort during our GPU port. However, RTS exhibits a wavefront data dependency pattern in its primary computational kernel as well as several blocking MPI communications. This section will focus on optimizing RTS while considering the complexities and limitations of the solver's underlying algorithm.

5.1 Summary of the Radiation Transport Solver

The MURaM code uses short characteristics to solve for the radiation field [27]. This method involves integrating the radiation transfer equation along a ray using values of intensity and opacity interpolated from the neighbouring grid cells. To calculate the mean intensity and radiative fluxes at each grid point a set of 3 rays per octant are used to integrate over the unit sphere. The solver uses

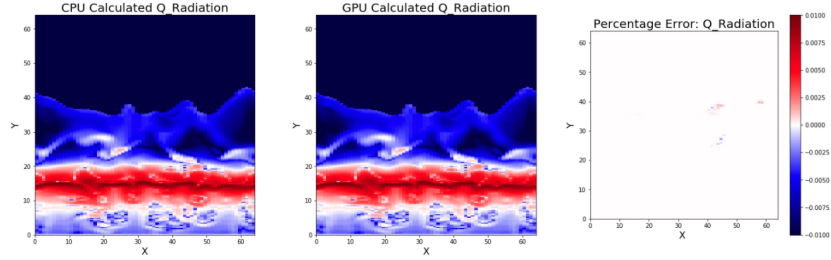


Figure 7: Percentage Error in GPU calculated $Q_{\text{Radiation}}$ after 50 iterations.

3D domain decomposition and iterates the intensities at the boundaries of each sub-domain until the errors are within a prescribed tolerance. A multi-band opacity scheme is used in order to efficiently include the frequency dependence of the radiation transfer problem in the solar atmosphere. For feedback into the MHD code the radiative heating or cooling at each point in space is calculated. In practice, using 3 rays per octant results in 24 total rays that are iteratively computed until they converge to an error threshold. Figure 8 shows the structure of the core computational loop in RTS. Expanding on the routines described in Section 2, `writebuf()` and `readbuf()` pack and unpack a buffer that will be exchanged with neighbors in the `exchange()` routine.

```

for( < x direction > )
for( < y direction > )
for( < z direction > )
for( < angle > ) // Total 24 rays
{
  interpol();
  while(g_maxerr > THRESHOLD)
  {
    readbuf();
    integrate();
    writebuf();
    exchange();
    double err = error();
    MPI_Allreduce(&err, &g_maxerr);
  }
  readbuf();
  flux();
}

```

Figure 8: Pseudocode of RTS’s core computational loop

The most important routine within RTS is called `integrate()`, which is executed 50-100 times per timestep. However, unlike the other routines, `integrate()` introduces a wavefront data dependency pattern that restricts the parallelism attainable within it. This means that even though we are working with a 3-dimensional domain, we can only achieve two dimensions of parallelism; one dimension of our problem will have to remain sequential as displayed in Figure 9.

This data dependency introduces several performance challenges that must be addressed: 1) GPU kernels with 2-D data parallelism are very small and under-utilize the compute processors of GPUs, 2) having one dimension of the domain remain sequential means we must launch possibly hundreds of small GPU kernels to compute the entire domain, introducing runtime-dominating kernel launch overhead, 3) since each ray sweeps in a different direction, some rays have better memory access striding than others, meaning that some rays take several times longer to compute than others.

5.2 Reducing Kernel Launch Overhead

Anytime a GPU kernel is launched a certain amount of overhead is incurred. When this overhead is very small compared to the time

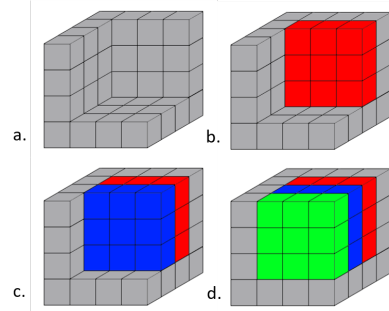


Figure 9: Representation of the wavefront dependency in RTS integration. a) shows the preloaded boundary conditions with no computation done. b) shows the first set of grid points in red to be computed in parallel. c) shows the next set of grid points to be computed in parallel, each blue grid point depends on up to four of the red grid points. d) shows the last grid points to be computed in parallel, each green grid point depends on up to four of the blue grid points.

spent in the GPUs parallel computation, good performance is still achieved. However, in edge-cases such as our `integrate()` routine, this overhead can become a dominant factor in the overall execution time. The OpenACC `async` directive can be used to hide a large portion of this overhead by queuing many kernels on the GPU before they are run. While the earlier kernels are being computed, the later kernels are being pre-loaded which allows overlap between the execution of the current kernel and the setup of the next one. However, by closely analyzing the GPU profiler, `nvprof`, it was clear that even with this optimization our `integrate()` routine was still performing sub-optimally due to kernel launch overhead.

Figure 10a shows the overhead between two launches of the `integrate()` kernel. Each of these kernels are only computing two dimensions of the dataset, and a single call to the `integrate()` routine will result in a few hundred of these kernels being launched. In between the computation of each kernel is $35\mu\text{s}$ where the GPU processors are idle. The profiler revealed that there is some amount of data movement happening before and after each kernel, and the source was a pointer translation. This is likely related to the host address pointer needing to be translated with the device address pointer within the OpenACC runtime.

To address this, we changed how the arrays in `integrate()` were being allocated; instead of allocating them on the host first then the device, we allocated them only on the device. The effect of this is seen in Figure 10b, where the overhead has been reduced to $26\mu\text{s}$ between kernels. This is an improvement, but the profiler

still clearly shows that something is still happening between these kernel launches. We found that this has something to do with how C++ class members are handled. Since all of the arrays used within RTS are stored within a class we created a pointer outside of a class that referenced the needed arrays, and used those new pointers in *integrate()*. After this change Figure 10c shows that the overhead is further reduced to 5 μ s between the kernels. This means that *integrate()* is still spending nearly half of its time with idle GPU processors. In order to address this issue, we would need to refactor the code as discussed in the next section.



Figure 10: Nvprof profiler highlights the process of reducing kernel launch overhead in the RTS *integrate()* kernel. (a) Overhead between 2 launches, (b) Reduced overhead between kernels launches, and (c) Further reduced overhead

5.3 Restructuring of RTS Integration

This section will discuss further RTS code optimizations that require refactoring the RTS code.

5.3.1 RTS Transpose. Since *integrate()* has to deal with a data dependency there are three possible scenarios that we refer to as an x, y or z dependency. These names depend on which of the three dimensions must remain sequential, as outlined in Figure 9. An x or y dependency are parallelized in such a way that the z direction is handled by the inner most loop, which allows for vectorization on a perfectly strided array. However, for the z dependency, the x direction is the inner most loop which results in very bad memory striding. The z dependency is up to 10x slower than x or y, depending slightly on the dataset. The domain decomposition and dataset dimensions will determine how often the rays exhibit the z dependency, and in typical runs it happens often.

Our solution to this was to create a second version of all of the arrays used within *integrate()* to have an alternate transposed version. This includes the intensity which is calculated within *integrate()* and the coefficients which is calculated within *interpol()*. *Interpol()* uses three other arrays to calculate the coefficients, but they are

read-only within *interpol()*. We transpose the three read-only arrays in *interpol()* once per timestep before the main computation happens, then we ensure that the coefficients are written in the same order that *integrate()* will read them. Then we transpose the intensity array back before the flux values are calculated.

This results in the *integrate()* kernel being able to work in perfect stride even when encountering a z dependency pattern. The cost is the few extra transposes that have to be done, but in our test runs we are still seeing a significant improvement with *integrate()* running 5x faster overall, and RTS as a whole running 3x faster. This is ultimately a performance loss for the CPU, but is easily manageable using branching compilation with `ifdef` in C++. This "data tranposition" version of RTS performed well for the GPU in every test case we have tried, so the results discussed in Section 6 use these changes.

5.3.2 RTS Integration and Interpolation Merge. One strategy for addressing the 50% idle time of *integrate()* is to increase the amount of computations performed in each kernel. The two kernels that can be most easily merged are *interpol()* and *integrate()*. However, as seen in Figure 8 *integrate()* is inside of a convergence while loop and *interpol()* is outside of it. This is because the coefficients calculated in *interpol()* only need to be done once for each ray and the results are stored within an array to be read from in *integrate()*. Instead of storing the coefficients into an array we moved their calculation into the *integrate()* kernel and used them directly. This means that any ray that takes more than one iteration to converge will now have to compute these coefficients more often, but with the possible benefit that now with more work to do the *integrate()* kernel may be more efficient.

The results of this change varied in our test cases. For smaller datasets, such as 64³, where the GPU occupancy was at its lowest and the kernel had less work to do, the *interpol()* and *integrate()* merge resulted a speedup of around 30% for RTS overall when compared to a GPU run without this change. This optimization might be beneficial for future MURaM forecasting scenarios, where high throughput (capability) would be of paramount importance, requiring strong scaling to smaller per-GPU problem sizes to achieve. However, problem sizes more representative of the current use of MURaM simulations showed a significant performance decrease of up to 50%.

In the chromosphere the radiation field can be strongly scattering, meaning the radiation source function is strongly dependent on the intensity. For strong-scattering problems, the radiation transfer problem becomes more non-local, increasing iterations to convergence. In this case it is preferable to use a Gauss-Seidel convergence scheme [46]. As the intensity is integrated along the ray, this scheme will require updating the source function for each point along the ray, and then using the 'new' source function to integrate the intensity at the next point along the ray. This algorithm requires a combined treatment of interpolation and integration. This modification will therefore be of interest to apply the GPU short-characteristics scheme to broader range of stellar problems. For this reason, this variation of RTS may be an important direction for future work.

5.3.3 Similar Dependency Overlap. Another challenge that we addressed was the low GPU occupancy observed in *integrate()*.

One technique tried was to combine the computation of several rays into a single kernel. Our first approach was to use OpenACC asynchronous programming to queue the work of all 24 rays simultaneously on the GPU. The hope was that the GPU would be able to overlap the computation of multiple rays since a single ray is only using about 10% of GPU resources.

In practice, we observed through the GPU profiler, `nvprof`, that this method did allow for a little bit of overlap between the computation of multiple rays, but far less than what we would assume to be theoretically possible. In our experimentation, this method only improved performance by 5%. Typically when OpenACC asynchronous programming, GPU computation overlaps with either CPU computation or CPU/GPU data transfers. Additionally, there is no way to lock specific streaming multiprocessors to specific kernels within OpenACC. If this existed it could possibly be a viable solution to the problem we are facing.

We have experimented with a few other optimization variations. First, instead of relying on the OpenACC `async` clause to overlap computation, rays that exhibit a similar dependency pattern are combined with an outer parallelizable loop. We can identify 6 groups with 4 rays each that will exhibit a similar dependency pattern with the group. This means that the arrays used within the affected RTS computation routines must be increased in size by a factor of 4. This would increase the work done per `integrate()` kernel by a factor of 4 as well. When only considering the computational benefits of this change we observed a reasonable performance benefit. And similar to the methodology in Section 5.3.2 this RTS variation received a larger performance increase for smaller datasets, likely when the idle time between kernels and GPU occupancy is at its lowest.

Since many rays would now be overlapped, instead of computed one-at-a-time, the way to determine convergence is changed to a global convergence instead of a per-ray convergence. This could have the added benefit of reducing the total number of iterations needed overall. Additionally, since 4 rays can be computed simultaneously, there will be 4 times fewer `exchange()` function calls and a factor of 24 times less `error()` function calls and associated MPI all-reduce routine calls which could greatly reduce the MPI communication overhead within RTS. Lastly, since half of the rays are moving upward and half moving downward it is possible that we could use 3 groups of 8 rays instead of 6 groups of 4, as rays moving upward vs. downward could still exhibit the same dependency pattern.

Implementing and evaluating these optimization ideas fully remains as future work for the project, and are not utilized when discussing performance results in this paper.

6 RESULTS

In this section, we present the results of running MURaM on multi-processor CPUs and GPUs while demonstrating parallel efficiency.

6.1 Experimental Setup

The Cobra system consists of 3424 compute nodes, each containing two Intel Xeon Gold 6148 Skylake (SKL) processors (20 cores at 2.4 GHz) and 100 Gb/s OmniPath interconnect. There are 64 GPU nodes with 2 NVIDIA Tesla V100-PCIe-32GB per node utilizing 32 GB HBM2 for a total of 7.9 TB HBM2 across all nodes. CPU runs: Intel 19.1.3, Intel MPI 2019.9, MKL 2020.2, FFTW-MPI 3.3.8.

GPU runs: For the -O0 runs - NVHPC 20.4, CUDA 10.2, OpenMPI 4.0.5 with UCX 1.8.0, FFTW-MPI 3.3.8; For the -O3 runs - NVHPC 20.9, CUDA 11, OpenMPI 4.0.5 with UCX 1.8.0 and FFTW-MPI 3.3.8. At the time of submission, we were able to collect results for GPU strong scaling for the 288^3 dataset using -O3. For the weak scaling, the runs used -O0 and the -O3 runs were finishing up. Preliminary results showed for the 288^3 dataset, with -O3, the GPU weak scaling ran approximately 10% faster. (Note: PGI compilers have been since October 2020 renamed to NVHPC [35])

6.2 Single GPU Performance

Our initial project focus was optimizing performance on a single GPU. In practice, the simulations that are run with MURaM will require multiple GPUs, but using a smaller dataset allows us to study GPU performance separately from the scalability of the MPI implementation. Using a single V100 GPU, the average time to simulate one single-band (or gray scale) timestep with the 288^3 dataset is 2.285 seconds. This is a 1.73x speedup over the 3.949 seconds required to run the same simulation on a fully subscribed 40-core Skylake CPU node.

6.3 Strong Scaling

Strong scaling is defined as how the solution time varies with the number of processors for a fixed total problem size. For our strong scaling experiment we use a 288^3 dataset divided across 8 GPUs and 8 fully subscribed CPU Skylake nodes (40-cores per node). The CPU runs use -O3 and AVX512 flags and the GPU runs use -O3. We are also comparing the strong scaling performance of the code with gray band (1 band) and colored band (4 band and 12 band). The colored band increases the workload in RTS and is proportional to the scaling of RTS. Figure 11 shows the strong scaling of MURaM with this configuration. The performance of the code is measured in millions of sites updates per second (Msite/s). Cobra contains 2 GPUs per node, so increasing to 4 GPUs requires inter-node communication. From 1 to 2 GPUs the code scales very well in both the single and 4-band case, roughly doubling the throughput. However, moving from 2 to 4 GPUs only increases throughput by 1.63, which is possibly due to the higher cost of internode communication. Preliminary results shown for the 8 GPU runs indicate that a more optimal core decomposition for multi-node scaling may be chosen after further testing.

We also gathered strong scaling results using up to 96 GPUs for a $288 * 576 * 576$ single-band dataset, as shown in Figure 12. These results show the strong scaling performance of the RTS routine as compared to the overall simulation: both seem to do reasonably well. The scaling efficiency of both RTS and the full model begin to decrease when the dataset is split over more than 32 GPUs, and the number of points per GPU falls below one million.

6.4 Weak Scaling

Weak scaling is defined as how the solution time varies with the number of processors for a fixed problem size per processor and gives a great deal of information about the MPI communication and overall scalability of the code. Figure 13 shows a breakdown of the GPU weak scaling with respect to the different routines of the code. This figure is also measured in terms of seconds per timestep.

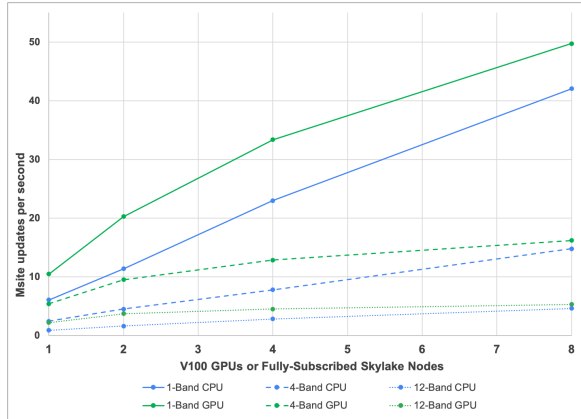


Figure 11: CPU-GPU strong scaling of a multi-band 288^3 dataset

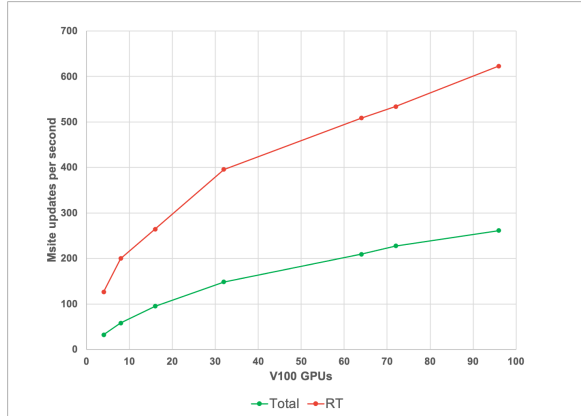


Figure 12: GPU Strong Scaling of a $288 \times 576 \times 576$ dataset

We use a 288^3 dataset per GPU for this experiment. It is clear that between 1 to 64 GPUs the scalability suffers due to the FFTW library. Currently, we are using multi-threaded FFTW on the CPU with results being copied to the GPU after computations. As a future direction, we plan to explore a GPU-enabled FFT library.

6.5 Results Summary

There is an increased computational cost moving the simulation from single-band to multi-band, as seen in Figure 11. For N-bands, the interpolation, integration, and flux calculation routines within RTS run N times more often. Additionally, there are differences in the convergence rate of RTS. Single-band RT is more transparent in the highly structured upper photosphere, resulting in good scaling in Figure 11. Multi-band RT is more sensitive to those structures and converges more slowly.

7 RELATED WORK

Accelerating the solar physics simulation models through GPU devices is a relatively new direction which attracts broad interest from the scientific community. Related work [9] shows the "Time-to-solution" performance results of a flux rope eruption simulation

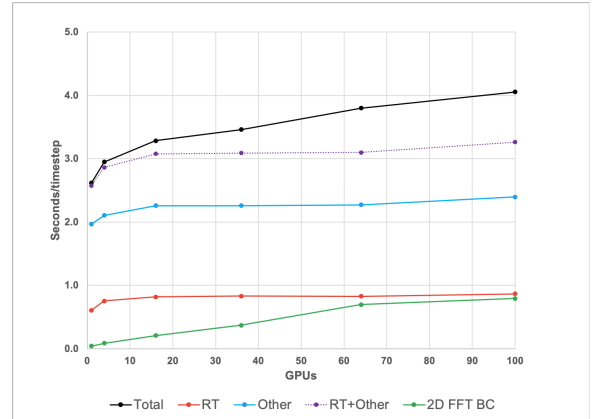


Figure 13: GPU weak scaling of a 288^3 dataset for RTS and other MURaM routines

with their OpenACC implementation of MAS code. MAS represents Magnetohydrodynamic Algorithm outside a Sphere(MAS), an in-production MHD code, which is part of the CORHEL suite hosted at the Community Coordinated Modeling Center (CCMC). Note that MHD is also a kernel in MURaM. The same group of researchers also summarized the implementation of OpenACC into MAS, including specific code example, strategies and development tips. Other non-GPU MHD codes include BATS-R-US [36] that solves 3D MHD equations in finite volume form using numerical method. The code uses Message Passing Interface (MPI) and the Fortran90 standard. Similarly PLUTO [31], a numerical code for computational astrophysics is a multi-physics, multi-algorithm, high resolution framework that comprises of MHD, which is one of the four independent physics modules of PLUTO.

As presented in this manuscript, one of the major kernels of interest to us in MURaM is the radiation transport. Related work include the recent acceleration of minisweep, a MiniApp of the Denovo [21] radiation transport application on GPUs [42, 43] using OpenACC. Results demonstrate that OpenACC running on NVIDIA's next-generation Volta GPU boasted an 85.06x speedup over serial code, which is larger than CUDA's 83.72x speedup over the same serial implementation. Other MiniApps demonstrating radiation transport approaches include Kripke [1] that uses RAJA [23] and Test-SNAP [45] (mimicking communication patterns of PARTISN [5] transport code) investigating different data layout patterns and parallelism using Kokkos and OpenMP offload model [20]. Coarray Fortran-based Sweep3D's comparable performance to that of the MPI is discussed in [15]. The work on Ardra [28] discusses porting discrete ordinate transport code to CUDA while using RAJA model with CHAI [25] and Umpire [6] to manage multiple memory spaces.

8 CONCLUSION

We have successfully added GPU acceleration to the MURaM code using OpenACC using a test-driven refactoring methodology. The refactored code achieves performance-portability between CPU and GPU, and with one exception (the RTS transposition optimization described in Section 5.3.1 above), is implemented as a single code-base. While our work represents a fully functional port of

MURaM to GPUs, not all of MURaM's routines have been fully optimized. Rather, we have focused here on a series of optimizations to RTS, the most expensive and therefore most critical routine to MURaM performance. Results for a 288^3 test problem show that MURaM with the optimized RTS routine achieves 1.73x speedup using a single NVIDIA V100 GPU over a fully subscribed 40-core Intel Skylake CPU node and with respect to the number of simulation points (in millions) per second, a single NVIDIA V100 GPU is equivalent to 69 Skylake cores. Multi-GPU weak scaling tests on Cobra show that all components of MURaM, with the exception of the 2D FFT call in BND, can be scaled out. This opens the door to MURaM experiments on large solar domains once a more scalable 2D FFT is identified and incorporated. Strong scaling tests illustrate the point that GPUs can run RTS with 4 frequency bands as fast or faster than comparable numbers of CPU nodes can run single band, enabling routine use of multi-band RTS in solar research. The OpenACC implementation will allow the MURaM code to utilize the latest state-of-the-art HPC multi-GPU systems deployed at various leadership-class centers around the world. We fully expect further improvements to the model's performance and scalability as our optimization focus widens to include other routines and as the next generation of GPUs are deployed.

REFERENCES

- [1] 2017. Kripke. (2017). . <https://codesign.llnl.gov/kripke.php> [Online; accessed 15-August-2017].
- [2] 2017. Solar Flares: From Emergence to Eruption. <https://news.ucar.edu/132648/emergence-eruption>. (2017).
- [3] 2020. PCAST — PGI Compiler Assisted Software Testing. <https://github.com/ORNL-CEES/Profugus>. (2020).
- [4] JA Aguilera and C Aragón. 2007. Multi-element Saha–Boltzmann and Boltzmann plots in laser-induced plasmas. *Spectrochimica Acta Part B: Atomic Spectroscopy* 62, 4 (2007), 378–385.
- [5] Randal S. Baker. 2014. PARTISN on Advanced/Heterogeneous Processing Systems. (2014). <http://permalink.llnl.gov/object/tr?what=info:llnl-repo/lareport/LA-UR-13-20948> [Online; accessed 24-June-2014].
- [6] D Beckingsale. 2017. Umpire. <https://umpire.readthedocs.io/en/develop/>. (2017).
- [7] Claudio Bonati, Enrico Calore, Massimo D’Elia, Michele Mesiti, Francesco Negro, Francesco Sanfilippo, Sebastiano Fabio Schifano, Giorgio Silvi, and Raffaele Tripiccone. 2018. Portable multi-node LQCD Monte Carlo simulations using OpenACC. *International Journal of Modern Physics C* 29, 01 (2018), 1850010.
- [8] Reuben D Budiardja and Christian Y Cardall. 2019. Targeting GPUs with OpenMP directives on Summit: A simple and effective Fortran experience. *Parallel Comput.* 88 (2019), 102544.
- [9] Ronald M Caplan, Jon A Linker, Zoran Mikić, Cooper Downs, Tibor Török, and VS Titov. 2019. GPU Acceleration of an Established Solar MHD Code using OpenACC. In *Journal of Physics: Conference Series*, Vol. 1225. IOP Publishing, 012012.
- [10] B. G. Carlson. 1963. The numerical theory of neutron transport. In *Methods in Computational Physics*, Vol. 1, B. Alder and S. Fernbach (Eds.), 1.
- [11] Sunita Chandrasekaran and Guido Juckeland. 2017. *OpenACC for Programmers: Concepts and Strategies*. Addison-Wesley Professional.
- [12] Barbara Chapman, Gabriele Jost, and Ruud Van Der Pas. 2008. *Using OpenMP: portable shared memory parallel programming*. Vol. 10. MIT press.
- [13] M. C. M. Cheung, M. Rempel, G. Chintzoglou, F. Chen, P. Testa, J. Martínez-Sykora, A. Sainz Dalda, M. L. DeRosa, A. Malanushenko, V. Hansteen, B. De Pontieu, M. Carlsson, B. Gudiksen, and S. W. McIntosh. 2019. A comprehensive three-dimensional radiative magnetohydrodynamic simulation of a solar flare. *Nature Astronomy* 3 (Nov. 2019), 160–166. <https://doi.org/10.1038/s41550-018-0629-3>
- [14] M. P. Clay, D. Buaria, and P. K. Yeung. 2017. Improving Scalability and Accelerating Petascale Turbulence Simulations Using OpenMP. <http://openmpcon.org/conf2017/program/>. (2017). To Appear.
- [15] Cristian Coarfa, Yuri Dotsenko, and John Mellor-Crummey. 2006. Experiences with Sweep3D implementations in Co-array Fortran. *The Journal of Supercomputing* 36, 2 (2006), 101–121.
- [16] Joshua Hoke Davis, Christopher Daley, Swaroop Pophale, Thomas Huber, Sunita Chandrasekaran, and Nicholas J Wright. 2020. Performance Assessment of OpenMP Compilers Targeting NVIDIA V100 GPUs. *arXiv preprint arXiv:2010.09454* (2020).
- [17] A. Dedner, F. Kemm, D. Kröner, C.-D. Munz, T. Schnitzer, and M. Wesenberg. 2002. Hyperbolic Divergence Cleaning for the MHD Equations. *J. Comput. Phys.* 175 (Jan. 2002), 645–673. <https://doi.org/10.1006/jcph.2001.6961>
- [18] Jose Monsalve Diaz, Kyle Friedline, Swaroop Pophale, Oscar Hernandez, David E Bernholdt, and Sunita Chandrasekaran. 2019. Analysis of OpenMP 4.5 Offloading in Implementations: Correctness and Overhead. *Parallel Comput.* 89 (2019), 102546.
- [19] DOE. 2020. The Compelling Case for Exascale Computing. <https://www.exascaleproject.org/>. (2020).
- [20] H Carter Edwards and Christian R Trott. 2013. Kokkos: Enabling performance portability across manycore architectures. In *2013 Extreme Scaling Workshop (xsw 2013)*. IEEE, 18–24.
- [21] Thomas M Evans, Wayne Joubert, Steven P Hamilton, Seth R Johnson, John A Turner, Gregory G Davidson, and Tara M Pandya. 2015. *Three-dimensional discrete ordinates reactor assembly calculations on GPUs*. Technical Report. Oak Ridge National Lab.(ORNL), Oak Ridge, TN (United States). Oak Ridge
- [22] Tobias Gysi, Carlos Osuna, Oliver Fuhrer, Mauro Bianco, and Thomas C Schulthess. 2015. STELLA: A domain-specific tool for structured grid methods in weather and climate models. In *Proceedings of the International Conference for High Performance Computing, Networking, Storage and Analysis*. 1–12.
- [23] Richard D Hornung and Jeffrey A Keasler. 2014. *The RAJA portability layer: overview and status*. Technical Report. Lawrence Livermore National Lab.(LLNL), Livermore, CA (United States).
- [24] The OpenACC Application Programming Interface. 2020. OpenACC 3.1. <https://www.openacc.org/sites/default/files/inline-images/Specification/OpenACC-3.1-final.pdf>. (2020).
- [25] H Jones, D Poliakkoff, and P Robinson. 2017. CHAI. <https://github.com/LLNL/CHAI>. (2017).
- [26] Jeongnim Kim, Andrew D Baczewski, Todd D Beaudet, Anouar Benali, M Chandler Bennett, Mark A Berrill, Nick S Blunt, Edgar Josué Landinez Borda, Michele Casula, David M Ceperley, et al. 2018. QMCPACK: an open source ab initio quantum Monte Carlo package for the electronic structure of atoms, molecules and solids. *Journal of Physics: Condensed Matter* 30, 19 (2018), 195901.
- [27] P. B. Kanasz and L. Auer. 1988. Short characteristic integration of radiative transfer problems: formal solution in two-dimensional slabs. *J. Quant. Spectrosc. Radiat. Transfer* 39 (1988), 67.
- [28] A Kunen, J Loffeld, A Black, R Chen, P Nowak, T Haut, T Bailey, P Brown, S Rennich, P Maginot, et al. 2019. *Porting 3D discrete ordinates sweep algorithm in ardra to CUDA*. Technical Report. Lawrence Livermore National Lab.(LLNL), Livermore, CA (United States).
- [29] JaeHyuk Kwack, Colleen Bertoni, Buu Pham, and Jeff Larkin. 2019. Performance of the RI-MP2 Fortran Kernel of GAMESS on GPUs via Directive-Based Offloading with Math Libraries. In *International Workshop on Accelerator Programming Using Directives*. Springer, 91–113.
- [30] Stefan Maintz and Markus Wetzstein. 2018. Strategies to accelerate VASP with GPUs using open ACC. *Proceedings of the Cray User Group* (2018).
- [31] Andrea Mignone, G Bodo, S Massaglia, Titos Matsakos, O Tesileanu, C Zanni, and Anthony Ferrari. 2007. PLUTO: a numerical code for computational astrophysics. *The Astrophysical Journal Supplement Series* 170, 1 (2007), 228.
- [32] A. Nordlund. 1982. Numerical simulations of the solar granulation. I – Basic equations and methods. *Astronomy & Astrophysics* 107 (1982), 1–10. http://adsabs.harvard.edu/cgi-bin/nph-bib_query?bibcode=1982A%26A...107....1N&db_key=AST
- [33] NSF. 2020. The Daniel K. Inouye Solar Telescope (DKIST). <http://dkist.nso.edu>. (2020).
- [34] NVIDIA. 2017. CUDA. <https://developer.nvidia.com/cuda-zone>. (2017).
- [35] NVIDIA. 2020. NVIDIA HPC SDK. <https://www.pgroup.com/index.htm>. (2020).
- [36] Kenneth G Powell, Philip L Roe, Timur J Linde, Tamas I Gombosi, and Darren L De Zeeuw. 1999. A solution-adaptive upwind scheme for ideal magnetohydrodynamics. *J. Comput. Phys.* 154, 2 (1999), 284–309.
- [37] M. Rempel. 2014. Numerical Simulations of Quiet Sun Magnetism: On the Contribution from a Small-scale Dynamo. *acm* 789, Article 132 (July 2014), 132 pages. <https://doi.org/10.1088/0004-637X/789/2/132> arXiv:astro-ph.SR/1405.6814
- [38] M. Rempel. 2017. Extension of the MURaM Radiative MHD Code for Coronal Simulations. *acm* 834, Article 10 (Jan. 2017), 10 pages. <https://doi.org/10.3847/1538-4357/834/1/10> arXiv:astro-ph.SR/1609.09818
- [39] M Rempel, M Schüssler, and M Knölker. 2009. Radiative magnetohydrodynamic simulation of sunspot structure. *The Astrophysical Journal* 691, 1 (2009), 640.
- [40] Sunil Sathe. 2016. Accelerating the ANSYS Fluent R18.0 Radiation Solver with OpenACC. <https://tinyurl.com/yacxh5g7>. (2016).
- [41] Will Sawyer, Guenther Zaengl, and Leonidas Linardakis. 2014. Towards a multi-node OpenACC Implementation of the ICON Model. In *EGU General Assembly Conference Abstracts*, Vol. 16.
- [42] Robert Searles, Sunita Chandrasekaran, Wayne Joubert, and Oscar Hernandez. 2018. Abstractions and Directives for Adapting Wavefront Algorithms to Future Architectures. In *Proceedings of the Platform for Advanced Scientific Computing Conference*. ACM, 4.

- [43] Robert Searles, Sunita Chandrasekaran, Wayne Joubert, and Oscar Hernandez. 2019. MPI+ OpenACC: Accelerating radiation transport mini-application, minisweep, on heterogeneous systems. *Computer Physics Communications* 236 (2019), 176–187.
- [44] The OpenMP API specification for parallel programming. 2020. OpenMP 5.1. <https://www.openmp.org/wp-content/uploads/OpenMP-API-Specification-5-1.pdf/>. (2020).
- [45] Aidan P Thompson, Laura P Swiler, Christian R Trott, Stephen M Foiles, and Garritt J Tucker. 2015. Spectral neighbor analysis method for automated generation of quantum-accurate interatomic potentials. *J. Comput. Phys.* 285 (2015), 316–330.
- [46] J Trujillo Bueno and P Fabiani Bendicho. 1995. A novel iterative scheme for the very fast and accurate solution of non-LTE radiative transfer problems. *The Astrophysical Journal* 455 (1995), 646.
- [47] Verónica G Vergara Larrea, Reuben D Budiardja, Rahulkumar Gayatri, Christopher Daley, Oscar Hernandez, and Wayne Joubert. 2020. Experiences in porting mini-applications to OpenACC and OpenMP on heterogeneous systems. *Concurrency and Computation: Practice and Experience* (2020), e5780.
- [48] A. Vögler, S. Shelyag, M. Schüssler, F. Cattaneo, T. Emonet, and T. Linde. 2005. Simulations of magneto-convection in the solar photosphere. Equations, methods, and results of the MURaM code. *A&A* 429 (Jan. 2005), 335–351. <https://doi.org/10.1051/0004-6361:20041507>
- [49] Zhifeng Yang, Milton Halem, Richard Loft, and Supreeth Suresh. 2019. Accelerating MPAS-A model radiation schemes on GPUs using OpenACC. *AGUFM 2019* (2019), A11A–06.